Dalton Transactions

ROYAL SOCIETY OF CHEMISTRY

PAPER

View Article Online
View Journal | View Issue

Cite this: *Dalton Trans.*, 2024, **53**, 19235

Beyond the triple bond: unlocking dinitrogen activation with tailored superbase phosphines†

Vilakkathala U. Krishnapriya[a,b] and Cherumuttathu H. Suresh *[b,c]

Activating atmospheric dinitrogen (N_2), a molecule with a remarkably strong triple bond, remains a major challenge in chemistry. This theoretical study explores the potential of superbase phosphines, specifically those decorated with imidazolin-2-imine ($(ImN)_3P$) and imidazolin-2-methylidene ($(ImCH)_3P$) to facilitate N_2 activation and subsequent hydrazine (H_2NNH_2) formation. Using density functional theory (DFT) at the M06L/6-311++G(d,p) level, we investigated the interactions between these phosphines and N_2. Mono-phosphine–N_2 complexes exhibit weak, noncovalent interactions (−0.6 to −7.1 kcal mol^{-1}). Notably, two superbasic phosphines also form high-energy hypervalent complexes with N_2, albeit at significantly higher energies. The superbasic nature and potential for the hypervalency of these phosphines lead to substantial N_2 activation in bis-phosphine–N_2 complexes, where N_2 is "sandwiched" between two phosphine moieties through hypervalent P–N bonds. Among the phosphines studied, only $(ImN)_3P$ forms an exothermic sandwich complex with N_2, stabilized by hydrogen bonding between the ImN substituents and the central N_2 molecule. A two-step, exothermic hydrogen transfer pathway from $(ImN)_3P$ to N_2 results in the formation of a bis-phosphine–diimine (HNNH) sandwich complex. Subsequent hydrogen transfer leads to the formation of a bis-phosphine–hydrazine (H_2NNH_2) complex, a process that, although endothermic, exhibits surmountable activation barriers. The relatively low energy requirements for this overall transformation suggest its potential feasibility under the optimized conditions. This theoretical exploration highlights the promise of superbase phosphines as a strategy for metal-free N_2 activation, opening doors for the development of more efficient and sustainable nitrogen fixation and utilization methods.

Received 23rd September 2024,
Accepted 1st November 2024

DOI: 10.1039/d4dt02703e

rsc.li/dalton

Introduction

Nitrogen, the most abundant element in the Earth's atmosphere, is vital for almost all organisms. Yet, these organisms cannot use this nitrogen directly, and hence, the activation of nitrogen is an essential process.[1–3] The high dissociation energy and the high HOMO–LUMO gap make the activation of dinitrogen under ambient temperature and pressure conditions extremely challenging.[4] Dinitrogen (N_2) is very unreactive due to its strong NN triple bond and even today, the celebrated Haber process is the only non-natural way to activate this bond to produce useful nitrogenous compounds.[5–8] The Haber process makes use of catalysts that accelerate the cleavage of the N–N bond and the process involves the reaction between hydrogen and nitrogen at a moderately elevated temperature and high pressure. Such a process is very energy intensive, whereas N_2 fixation occurs under mild conditions naturally in some microorganisms by using the nitrogenase enzyme. The nitrogenase enzyme contains an Fe–Mo–S cluster complex, known as MoFe nitrogenase, where N_2 binds and gets reduced to ammonia.[9–12] While numerous studies have investigated the mechanism of N_2 activation by nitrogenase, the precise molecular details remain elusive.[13–19]

The presence of vacant and filled d orbitals of appropriate energy and symmetry of transition metal complexes allows them to accept and back-donate the electron density with N_2. This back-bonding weakens the highly stable N–N triple bond and is able to perform N_2 activation. Main group elements, lacking such d orbitals, have traditionally been less effective in N_2 activation. However, recent research has challenged this view, demonstrating the potential of metal-free catalysts for this crucial process. Extensive efforts have led to the development of various catalysts for N_2 activation, including those based on transition metals (Fe, Mo, Au, *etc.*), main group

[a]*Chemical Science and Technology Division, CSIR-National Institute of Interdisciplinary Science and Technology, Thiruvananthapuram – 695019, Kerala, India*
[b]*Research Centre, University of Kerala, Thiruvananthapuram, 695034 Kerala, India. E-mail: sureshch@gmail.com, sureshch@niist.res.in*
[c]*Srinivasa Ramanujan Institute for Basic Sciences, Kerala State Council for Science Technology and Environment, Kottayam, 686501 Kerala, India*

† Electronic supplementary information (ESI) available. See DOI: https://doi.org/10.1039/d4dt02703e

metals (Bi, Si, *etc.*), and, more recently, metal-free systems.[20–29] In the past three years, electrochemical ammonia production by main group metal-based catalysts has attracted greater attention in the field of N_2 activation.[6,30–33] While innovative approaches like electrochemical ammonia production and (photo)electrocatalysis have shown promise, progress has been hampered by reproducibility issues.[34]

Despite the predominance of metal-based catalysts, metal-free systems are gaining interest. In 2017, Bettinger *et al.* reported the photochemical extrusion of dinitrogen using phenylborylene under matrix isolation conditions.[35] Braunschweig *et al.* reported that dinitrogen can easily be reduced by using borylene.[36] Their work provides a pivotal moment in the scenario of dinitrogen activation using p-block elements and also offers that main group elements are also able to contribute in dinitrogen activation. Recently, p-block half-metal boron was found to be useful for the activation of N_2.[37] Among s-block elements, Li shows reactivity with N_2 because of its extreme reduction potential.[38,39] In 2021, Frenking *et al.* reported that low-valent Ca complexes can reduce dinitrogen.[39] The exceptional durability and activity of metal-free catalysts, coupled with their economic and environmental benefits, underscore the importance of their development. Consequently, there is a growing emphasis on the design and synthesis of novel metal-free catalysts for N_2 activation.

Very recently, Suresh and Krishnapriya[40] showed the remarkable electron-donating properties of the moieties imidazolin-2-imine (ImN–), its methyl derivative (Im′N–), imidazolin-2-methylidene (ImCH–) and its methyl derivative (Im′CH–). These moieties substituted to benzene, pyridine, N-heterocyclic carbene and phosphine led to the design of extremely electron-rich ligands. Fareed and Suresh also showed that substitution of such moieties on the phenyl ring (Fig. 1b and c) can lead to more than a 4-fold increase in cation–π interaction energy compared to benzene.[41] Dielmann *et al.* synthesized a variety of ImN-decorated extremely electron-rich phosphines.[42] Such nonionic phosphorus(III) ligands showed superior electron donating ability to any other known phosphines in chemistry and they are described as a new class of superbases. Dielmann *et al.* investigated their unique electron-releasing character to describe their capability to capture and cleave CO_2 molecules.[43] With their superior electron-donating ability towards a core structure, these moieties are promising candidates in homogeneous catalysis, offering innovative possibilities for creating auxiliary ligands and advancing catalysis research.

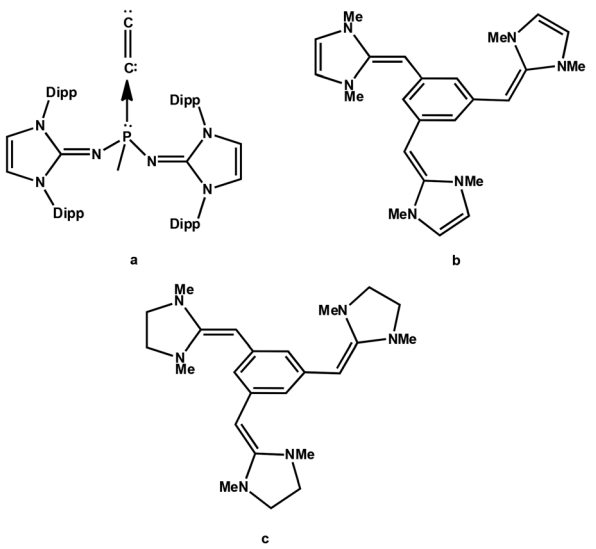

Fig. 1 (a) C_2 complex of the phosphine ligand synthesized by Leung *et al.* in 2021. (b) and (c) The cation–π receptors proposed by Fareed and Suresh in 2011.

Recently, the diatomic molecule C_2 has been structurally characterized by Leung *et al.* as a monoligated complex with the formula $(Im^aN)_2(CH_3)PC_2$ (Fig. 1a), where the N center of the imidazolidin-2-iminato groups (Im^aN) is adorned with the bulky R group 2,6-diisopropylphenyl.[44] Leung *et al.*'s discovery of a C_2 complex of phosphine suggests an unprecedented reaction in chemistry and the driving force of this reaction could be attributed to the incredible electron-donating properties of the Im^aN substituent which creates an extremely electron-rich phosphorus center in chemistry. The analysis of the electronic structure of $(Im^aN)_2(CH_3)PC_2$ with quantum chemical methods suggested the formation of the ligand-to-C_2 ($L \rightarrow C_2$) coordination bond which induced a large charge migration from P towards C_2. Despite the fact that ImCH- or Im'CH-based systems are yet to be synthesized, theoretical studies from our group suggest that phosphines decorated with these substituents are highly electron rich and they would behave as superbases (Fig. 2).

The focus of this study is on the metal-free N_2 activation reactions facilitated by the superbases of $(ImN)_3P$ and $(ImCH)_3P$ types. The study will assess the electron richness of these ligands and investigate the formation of both $L \rightarrow N_2$ and $L \rightarrow N_2 \leftarrow L$ complexes. We anticipate that the ability of phosphorus to achieve a hypervalent state will be key to the N_2 activation process.

The molecular electrostatic potential (MESP) is a valuable tool in computational chemistry for visualizing and understanding the distribution of the electron density within a molecule.[45–47] It provides insights into the regions of electrophilic and nucleophilic reactivities, intermolecular interactions, and the nature of chemical bonding.[48–51] In this study, MESP topological analysis is employed to assess the electron richness of superbase ligands and to visualize changes in electron density distribution during the N_2 activation process.

Computational methodology

All the computational calculations have been carried out with density functional theory (DFT) using Gaussian16 suites of programs.[52] All the ligands and complexes were optimized using the DFT method M06L/6-311++G(d,p).[53] Vibrational fre-

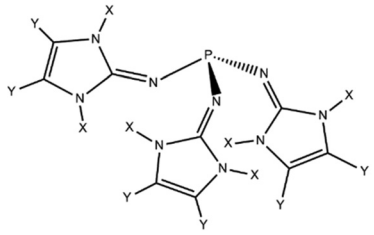

$(Im^aN)_3P$ X, Y = H
$(Im^bN)_3P$ X = H, Y = CH_3
$(Im^cN)_3P$ X = CH_3, Y = H
$(Im^dN)_3P$ X = CH_3, Y = CH_3

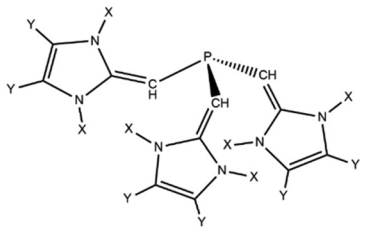

$(Im^aCH)_3P$ X, Y = H
$(Im^bCH)_3P$ X = H, Y = CH_3
$(Im^cCH)_3P$ X = CH_3, Y = H
$(Im^dCH)_3P$ X = CH_3, Y = CH_3

Fig. 2 Superbase phosphine ligands.

quency analysis has been carried out to ensure that all of the optimized strictures correspond to the local minima containing only positive vibrational frequencies. The energy difference between the complexes and the individual molecules optimized at the same level of theory is considered as the interaction energy of the complex. The self-consistent reaction field (SCRF) approach with the solvation model density (SMD) method was used to calculate the solvation-corrected energy change and free energy change. Non-polar acetonitrile was employed as the solvent for the calculation. Natural bond orbital (NBO) analysis[54,55] was employed to interpret bonding.

The MESP topological analysis was performed on the optimized geometries at the M06L/6-311++G(d,p) level of theory using the 'cube' and 'potential' keywords in Gaussian16. The MESP $V(\mathbf{r})$ at any point with respect to the position vector $\mathbf{r}$ is defined as follows:

$$V(\mathbf{r}) = \sum_{A}^{N} \frac{Z_A}{|\mathbf{r} - \mathbf{R}_A|} - \int \frac{\rho(\mathbf{r}')d^3r'}{|\mathbf{r} - \mathbf{r}'|}$$

where Z_A is the nuclear charge of atom A located at R_A and $\rho(\mathbf{r}')$ is the continuous electron density of the molecule and N is the total number of nuclei.[46,56] At the critical point, all the first-order derivatives of $V(\mathbf{r})$ vanish ($\Delta V(\mathbf{r}) = 0$). The eigenvalues of the Hessian matrix of the MESP minimum V_{min} shows three positive values and hence is known as the (3 + 3) critical point.[46,57–59] The MESP analysis is particularly used to depict significant changes in the lone pair region. Generally, electron-rich sites like π-regions and lone pair regions are associated with negative V_{min} values.

Results and discussion

MESP analysis of phosphines

Fig. 3 illustrates the depiction of V_{min} in the lone pair region of P in MESP isosurface plots for a representative set of PR_3 ligands. Considering the V_{min} of PH_3 of –23.6 kcal mol^{-1} as a reference point, the higher negative V_{min} of −39.0 kcal mol^{-1} observed for PMe_3 suggests that the methyl substitution on P leads to an increase in electron density around the lone pair region of P.

The introduction of imidazolin-2-imine (ImN–) and imidazolin-2-methylidene (ImCH–) moieties has been proposed as a strategy to design highly electron-rich substrates and ligands, leading to the classification of such ligands as superbases.[40,60] Compared to PMe_3, the superbases constructed through substitution with ImN–, Im′N–, ImCH–, and Im′CH– exhibit a notable increase in the magnitude of V_{min}. For example, considering the V_{min} values (Table 1), $P(Im^dN)_3$ emerges as the most electron-rich, demonstrating a 2.6-fold higher magnitude for V_{min} compared to PH_3, highlighting its exceptional electron richness. Previous studies have suggested that this new class of superbase phosphine ligands possesses an electron-donating ability comparable to that of N-heterocyclic carbenes.[40]

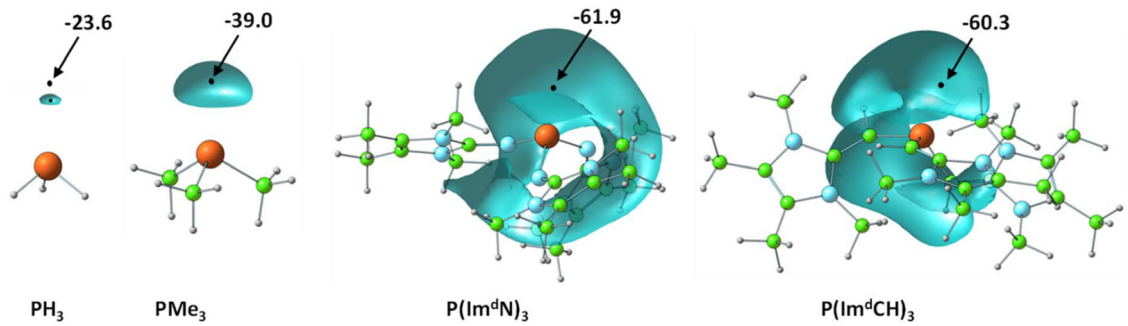

Fig. 3 Representation of the MESP isosurfaces of a set of phosphines at −20 kcal mol^{-1}. V_{min} values are given in kcal mol^{-1}. Color code: blue, N; green, C; grey, H; rust brown, P.

Table 1 MESP data of the phosphine ligands at the M06L/6-311++G(d,p) level of theory. V_{min} values are given in kcal mol^{-1}

Phosphine	V_{min}	Phosphine	V_{min}
PH_3	−23.6	$P(Im^dN)_3$	−61.9
PMe_3	−39.0	$P(Im^aCH)_3$	−50.8
$P(Im^aN)_3$	−47.6	$P(Im^bCH)_3$	−59.2
$P(Im^bN)_3$	−52.7	$P(Im^cCH)_3$	−59.6
$P(Im^cN)_3$	−56.8	$P(Im^dCH)_3$	−60.3

Mono-phosphine–N_2 complexes

The optimized structure of all $R_3P\cdots N_2$ complexes showed that the interaction of N_2 with phosphine is very weak, characterized as van der Waals-type interactions with P⋯N distances spanning from 3.44 to 4.43 Å. The respective interaction energies (Table S1†) fall within the range −0.6 to −7.1 kcal mol^{-1}, with the weakest observed for the $H_3P\cdots N_2$ complex and the strongest for the **$(Im^bN)_3P\cdots N_2$** complex. As a representative example, the optimized structure of **$(Im^bN)_3P\cdots N_2$** is shown in Fig. 4. Comparison with the free $(Im^bN)_3P$ ligand confirms that this weak N_2 complexation does not significantly perturb the phosphine's structure.

We further investigated complex formation involving a direct bond between the phosphorus of PR_3 and the nitrogen of N_2. Among all phosphines studied, only $P(Im^cN)_3$ and $P(Im^dN)_3$ showed the formation of such complexes with N_2. These complexes, denoted as **$(Im^cN)_3P–N_2$** and **$(Im^dN)_3P–N_2$**, are also depicted in Fig. 4. It is evident from the P–N distances that the P center forms bonds with five N centers, establishing the complex as a hypervalent phosphorus system. Notably, two of these P–N bonds are significantly shorter than those in free PR_3, while another two exhibit nearly identical distances. Only one P–N bond is elongated by approximately 0.1 Å compared to free phosphine. The N–N distance of 1.28 Å clearly indicates substantial dinitrogen activation due to the hypervalent bonding with the phosphine ligand. However, the energetics suggest that both **$(Im^cN)_3P–N_2$** and **$(Im^dN)_3P–N_2$** are high-energy systems, lying 70.1 and 65.9 kcal mol^{-1}, respectively, above free phosphine and N_2. Therefore, their formation under ambient conditions is unlikely.

Bis-phosphine–N_2 complexes

Fig. 5 presents the representative structures of bis-phosphine–N_2 complexes: Me_3P–NN–PMe_3 and **$(Im^aN)_3P–NN–P(Im^aN)_3$**. Notably, **$Me_3P–NN–PMe_3$** is 49.7 kcal mol^{-1} higher in energy, whereas **$(Im^aN)_3P–NN–P(Im^aN)_3$** is 18.1 kcal mol^{-1} lower in energy (ΔE) compared to free phosphines and N_2. In contrast, the formation of H_3P–NN–PH_3 is endothermic by 87.4 kcal mol^{-1}. This highlights the crucial role of the superbase character of $P(Im^aN)_3$ in enhancing the ligand's affinity for bonding with N_2. All bis-phosphine–N_2 complexes feature P–N bond formation from both ligands (Table 2). The P–NN distances fall within the range of 1.59–1.65 Å, significantly shorter than the typical range for a P–N single bond (1.70–1.77 Å). This suggests considerable double bond character in the P–NN bonds, implying hypervalency at the P center. Additionally, the N–N dis-

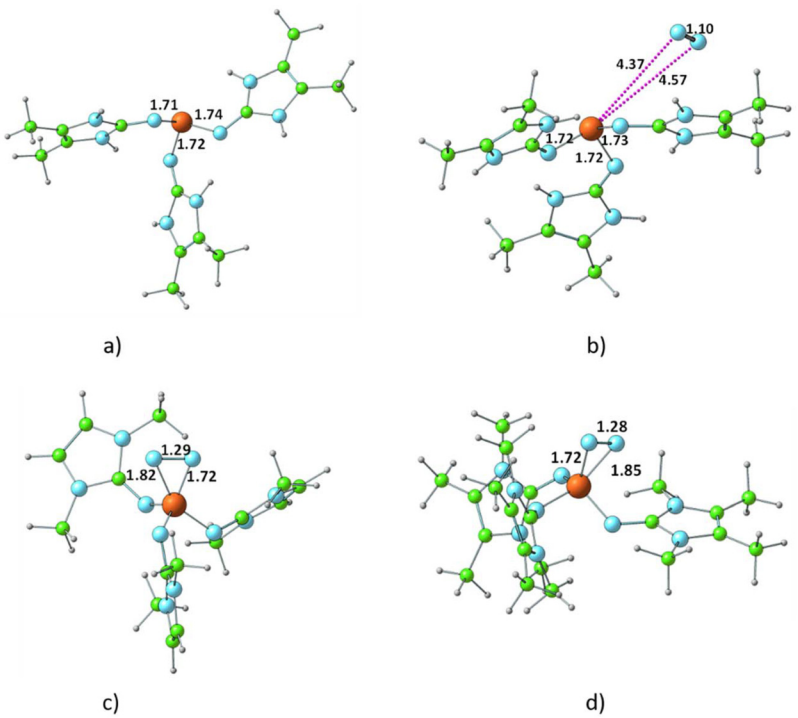

Fig. 4 Optimized structures of (a) the phosphine ligand $(Im^bN)_3P$, (b) the van der Waals complex **$(Im^bN)_3P\cdots N_2$**, and (c) and (d) the hypervalent complexes **$(Im^cN)_3P–N_2$** and **$(Im^dN)_3P–N_2$** at the M06L/6-311++G(d,p) level of theory.

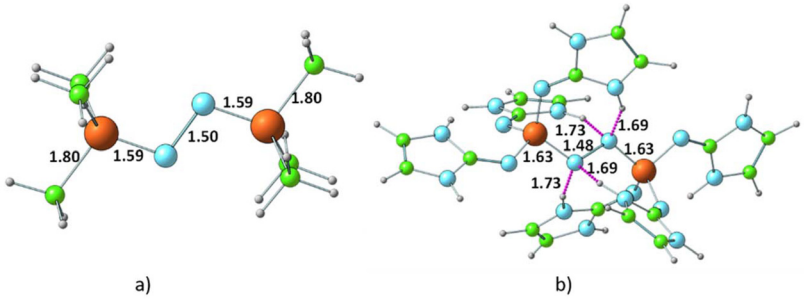

Fig. 5 Optimized structures of the dinitrogen bonded complexes of (a) PMe_3 and (b) $P(Im^aN)_3$ ligands. Bond distances and N···HN hydrogen bond distances are shown in Å.

Table 2 Structural and energetic data of the bis-phosphine–N_2 complexes at the M06L/6-311++G(d,p) level of DFT. Energy values are given in kcal mol^{-1} and distances are given in Å

Complex	ΔE	ΔG	D_{P-N1}	D_{P-N2}	D_{N-N}
$H_3P–NN–PH_3$	87.4	111.2	1.59	1.59	1.46
$Me_3P–NN–PMe_3$	49.7	72.4	1.59	1.59	1.50
$(Im^aN)_3P–NN–P(Im^aN)_3$	−13.3	18.5	1.63	1.63	1.48
$(Im^bN)_3P–NN–P(Im^bN)_3$	−18.1	18.4	1.61	1.62	1.47
$(Im^cN)_3P–NN–P(Im^cN)_3$	13.5	51.0	1.61	1.61	1.47
$(Im^dN)_3P–NN–P(Im^dN)_3$	2.6	42.3	1.60	1.62	1.46
$(Im^aCH)_3P–NN–P(Im^aCH)_3$	5.1	35.2	1.65	1.65	1.49
$(Im^bCH)_3P–NN–P(Im^bCH)_3$	41.1	68.1	1.61	1.62	1.46
$(Im^cCH)_3P–NN–P(Im^cCH)_3$	22.1	53.1	1.64	1.64	1.43
$(Im^dCH)_3P–NN–P(Im^dCH)_3$	20.2	55.4	1.63	1.63	1.44

tances range from 1.43 to 1.49 Å, approaching that of an N–N single bond. These data underscore the strength of the newly formed P–NN bonds, leading to a significant activation of the N≡N triple bond, effectively reducing it to an N–N single bond.

The energetics of the mono- and bis-phosphine complexes, summarized in Fig. 6, clearly demonstrate the superior N_2 activation capability of phosphine superbases bearing ImN-type substituents on phosphorus compared to those with ImCH-type substituents. Notably, the formation of $(Im^aN)_3P–NN–P(Im^aN)_3$ and $(Im^bN)_3P–NN–P(Im^bN)_3$ is exothermic, releasing 13.3 and 18.1 kcal mol^{-1}, respectively. This favorable energetic profile can be attributed to the additional stabilization provided by four N–H···N hydrogen bonds that surround the central N_2 unit (Fig. 5b), a feature unique to these systems possessing N–H bonds.

In the bis-phosphine–N_2 complex, dinitrogen is positioned between two phosphine moieties, forming two P–N bonds. This arrangement significantly alters the bonding environment at both the phosphorus and nitrogen centers. For instance, the three P–N bonds in $P(Im^aN)_3$ contract from 1.74,

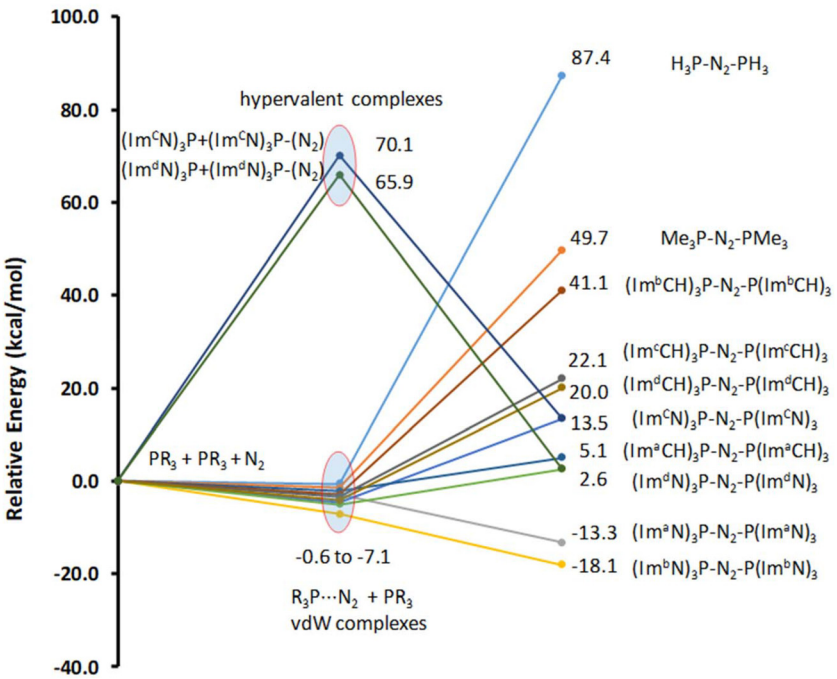

Fig. 6 Relative energies of the mono phosphine and bis-phosphine complexes with N_2. Energy data are given in kcal mol^{-1}.

1.71, and 1.72 Å to 1.69, 1.65, and 1.65 Å in the $(Im^aN)_3P–NN–P(Im^aN)_3$ complex, signifying stronger P–N bonds in the complex. Moreover, the two newly formed P–N bonds with N_2 exhibit an even shorter bond length of 1.63 Å. These structural data unequivocally demonstrate that all five P–N bonds in the hypervalent bis-phosphine–N_2 complex are substantially stronger than a typical P–N single bond. In essence, the remarkable hypervalent P–N bonding facilitates the activation of the N_2 triple bond, effectively reducing it to an N–N single bond.

The P–N bonding in the bis-phosphine–N_2 complex was further elucidated through NBO analysis, using $Me_3P–NN–PMe_3$ as a representative case. NBOs reveal that the N centers adopt an sp^2 hybridized state (Fig. 7). Degenerate NBOs 1 and 2, depicted in Fig. 7, represent π-bonds between P and N, arising from the interaction of the lone pair on N (the 'p' orbital not involved in sp^2 hybridization) with the Rydberg 'd' orbitals of the P center. This π-bonding interaction is predominantly contributed by the N center (89%), with the remaining contribution from the P center. Similarly, the degenerate NBOs 3 and 4 correspond to sp^2 hybrid lone pair orbitals on each N centers. The NBO 5 describes the N–N σ-bond formed from the sp^2 hybrid orbitals on the N centers. The degenerate NBOs 6 and 7 depict the σ-bonding orbitals between the third sp^2 hybrid orbital of the N center and primarily the 3s orbital of the P center.

NBO analysis and the observed N–N bond lengths collectively confirm the reduction of the N–N bond to a single bond

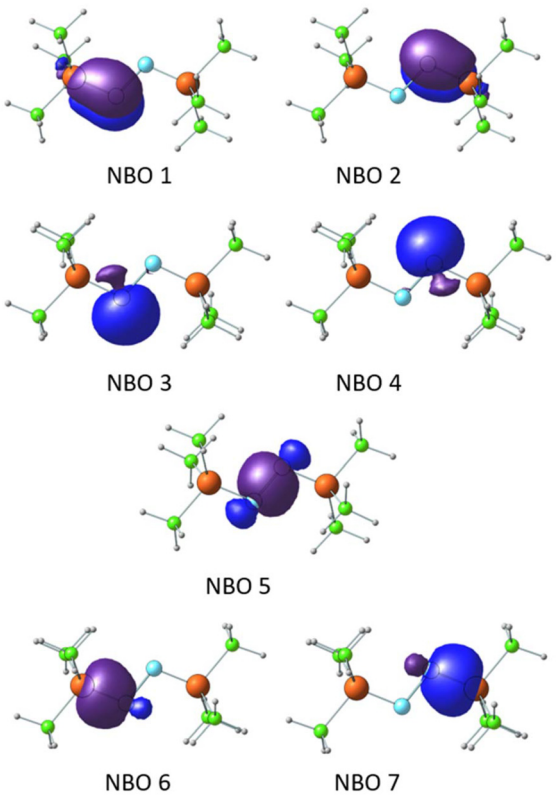

Fig. 7 Natural bond orbitals displaying the PN and NN bonding and lone pair orbitals.

character in the bis-phosphine–N_2 complexes. The calculated energy required for homolytic fission of $Me_3P–NN–PMe_3$ into two $Me_3P–N^{\bullet}$ radical fragments (66.1 kcal mol^{-1}) and the analogous process for $(Im^aN)_3P–NN–P(Im^aN)_3$ (75.3 kcal mol^{-1}) reveal a dramatic weakening of the N–N bond compared to its strength in dinitrogen (226 kcal mol^{-1}). This substantial decrease in bond strength underscores the remarkable activation of N_2 achieved through the formation of these hypervalent sandwich complexes with superbase phosphines.

The subsequent investigation, focusing on further N_2 activation, will exclusively consider $(Im^aN)_3P–NN–P(Im^aN)_3$ due to its exothermic formation and the presence of stabilizing N–H···N hydrogen bonds.

Formation of the diimine complex $(Im^aN')_3P–NHNH–P(Im^aN')_3$

Within the $(Im^aN)_3P–NN–P(Im^aN)_3$ complex, two of the four NN···HN hydrogen bonds are notably shorter (by 0.039 Å), suggesting the potential for further N_2 activation. This activation is realized through the transfer of a hydrogen atom involved in one of these shorter hydrogen bonds to the NN unit, yielding the NNH···N hydrogen-bonded intermediate $(Im^aN')_3P–NNH–P(Im^aN)_3$. The $(Im^aN')_3P$ ligand represents the "hydrogen abstracted" state of the original $(Im^aN)_3P$ ligand. This hydrogen transfer proceeds *via* the transition state ts1, characterized by the partial formation of an NN–H bond concurrent with the rupturing of the original H–N bond. The resulting intermediate, $(Im^aN')_3P–NNH–P(Im^aN)_3$, features four hydrogen bonds surrounding the 'NNH' unit (Fig. 8). Subsequent activation of the N–N bond occurs through another hydrogen transfer involving the shortest of these hydrogen bonds (HNN···HN, 1.638 Å), leading to the transition state ts2. The final product is a sandwich complex of diimine (HNNH) with the phosphine ligand $(Im^aN')_3P$, namely $(Im^aN')_3P–HNNH–P(Im^aN')_3$.

The solvation energy-incorporated energy profile diagram for the hydrogen transfer within the $(Im^aN)_3P–NN–P(Im^aN)$ complex, leading to the activated diimine product $(Im^aN')_3P–HNNH–P(Im^aN')_3$, is presented in Fig. 9. This process involves two exothermic (and exergonic) hydrogen transfer steps. The initial hydrogen transfer, exothermic by 6.1 kcal mol^{-1}, proceeds through ts1 with an activation energy of only 2.6 kcal mol^{-1}. The resulting intermediate, $(Im^aN')_3P–NNH–P(Im^aN)_3$, then undergoes a second hydrogen transfer *via* ts2. This step, with an activation barrier of 1.0 kcal mol^{-1}, is even more exothermic, releasing 14.1 kcal mol^{-1}. Overall, the reaction is exothermic by 20.2 kcal mol^{-1}. When considering the free energy profile, both steps appear virtually barrierless, and the formation of the diimine complex $(Im^aN')_3P-NHNH-P(Im^aN')_3$ is exergonic by 18.0 kcal mol^{-1}.

$$(Im^aN')_3P–HNNH–P(Im^aN')_3 \rightarrow 2\ (Im^aN')_3P–HN^{\bullet} \quad (1)$$

The N–N bond strength of the diimine complex $(Im^aN')_3P–HNNH–P(Im^aN')_3$ was evaluated through the energetics of reaction (1). Cleavage of the N–N bond, yielding the radical $(Im^aN')_3P–HN^{\bullet}$, requires a dissociation energy of 45.6 kcal mol^{-1}, highlighting the significant activation of the N–N bond.

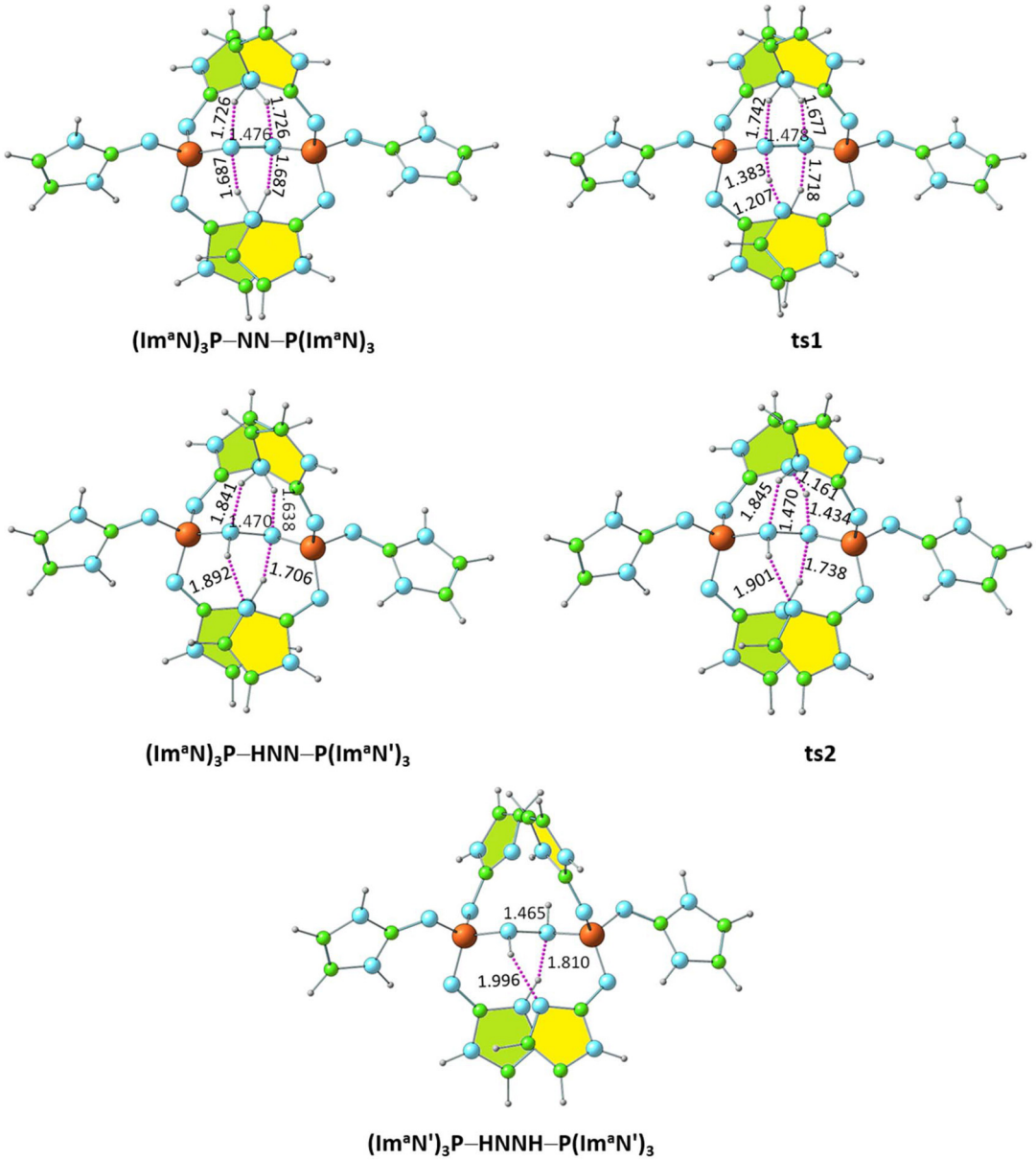

Fig. 8 Optimized structures of the products and transition states for the formation of the diimine complex **(Im^{a}N′)$_3$P–HNNH–P(Im^{a}N′)$_3$**. P–N and N–N distances are shown in Å.

Notably, the N–N bond in the diimine is weakened by 29.7 kcal mol^{-1} compared to that observed in the dinitrogen complex **(Im^{a}N)$_3$P–NN–P(Im^{a}N)$_3$**.

Hydrazine complex (Im^{a}N″)$_3$P–H$_2$NNH$_2$–P(Im^{a}N″)$_3$

Further activation of the N–N bond in the diimine complex can lead to the formation of a hydrazine complex, **(Im^{a}N″)$_3$P–H$_2$NNH$_2$–P(Im^{a}N″)$_3$**, *via* hydrogen transfer reactions (Fig. 10). Here, the (Im^{a}N″)$_3$P ligand represents the "hydrogen abstracted" state of the (Im^{a}N′)$_3$P ligand. The N–H···N hydrogen bond (1.810 Å) observed in **(Im^{a}N′)$_3$P–HNNH–P(Im^{a}N′)$_3$** is considered for the initial hydrogen transfer reaction. This process proceeds through the transition state ts3, yielding the intermediate **(Im^{a}N″)$_3$P–H$_2$NNH–P(Im^{a}N″)$_3$**.

The solvation-corrected energy and free energy profiles (Fig. 11) reveal that this reaction has an activation energy of 8.6 kcal mol^{-1} and an activation free energy of 6.7 kcal mol^{-1}. It is also endothermic by 7.0 kcal mol^{-1} and endergonic by 9.8 kcal mol^{-1}.

A subsequent hydrogen transfer within the intermediate **(Im^{a}N″)$_3$P–HNNH$_2$–P(Im^{a}N′)$_3$** leads to the hydrazine complex **(Im^{a}N″)$_3$P–H$_2$NNH$_2$–P(Im^{a}N″)$_3$** *via* ts4. This step exhibits activation energies of 11.3 kcal mol^{-1} (energy) and 6.6 kcal mol^{-1} (free energy). Overall, the formation of the hydrazine complex from the diimine complex is endothermic by 15.8 kcal mol^{-1} and endergonic by 16.1 kcal mol^{-1}. However, both the activation energy and activation free energy are readily surmountable under ambient conditions.

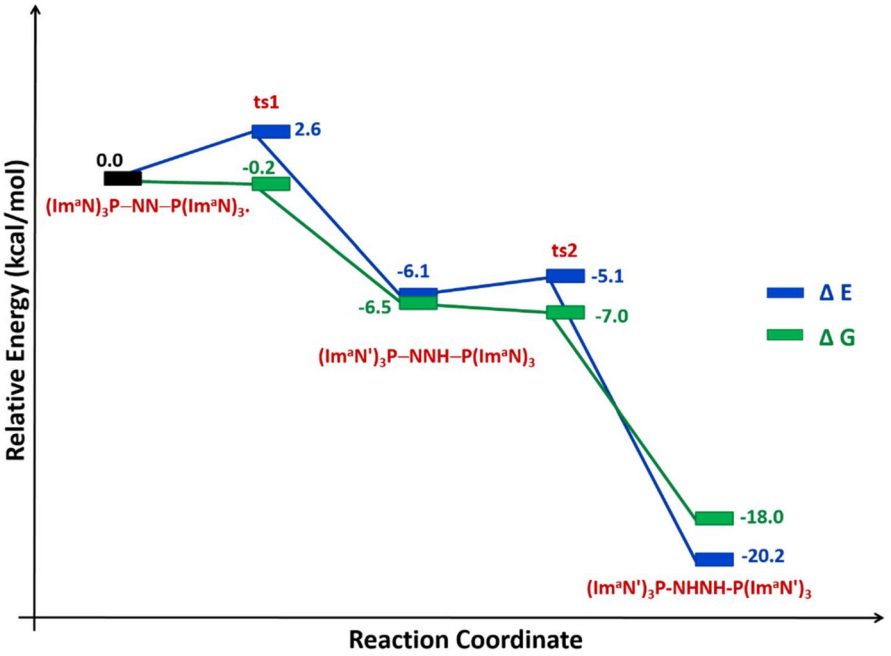

Fig. 9 Reaction energy profile diagram for hydrogen transfer occurs in $(Im^aN)_3P–NN–P(Im^aN)_3$ to form the diimine complex $(Im^aN')_3P–HNNH–P(Im^aN')_3$.

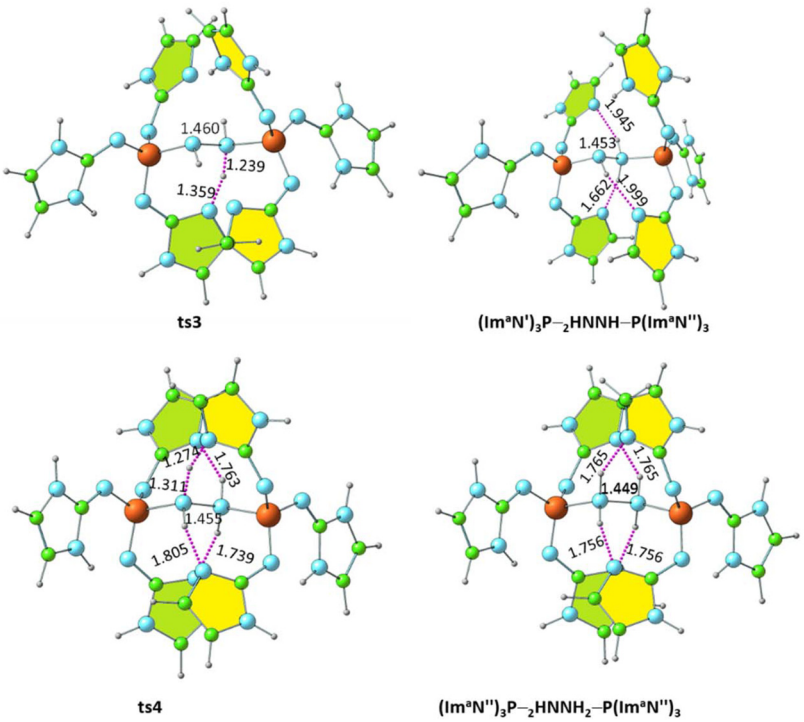

Fig. 10 Optimized structures of the products and transition states for the formation of the hydrazine complex $(Im^aN'')_3P–H_2NNH_2–P(Im^aN'')_3$. P–N and N–N distances are shown in Å.

We also modelled the dissociation of both $(Im^aN'')_3P$ ligands from the hydrazine complex $(Im^aN'')_3P–H_2NNH_2–P(Im^aN'')_3$ to generate the hydrazine H_2NNH_2. Since two P–N bonds are cleaved in this dissociation, a stepwise dissociation is considered. The first P–N bond dissociation (reaction (2)) occurs with an energy change of 30.9 kcal mol^{-1} and a free energy change of 15.2 kcal mol^{-1}. The second P–N bond dissociation, releasing hydrazine (reaction (3)), occurs from

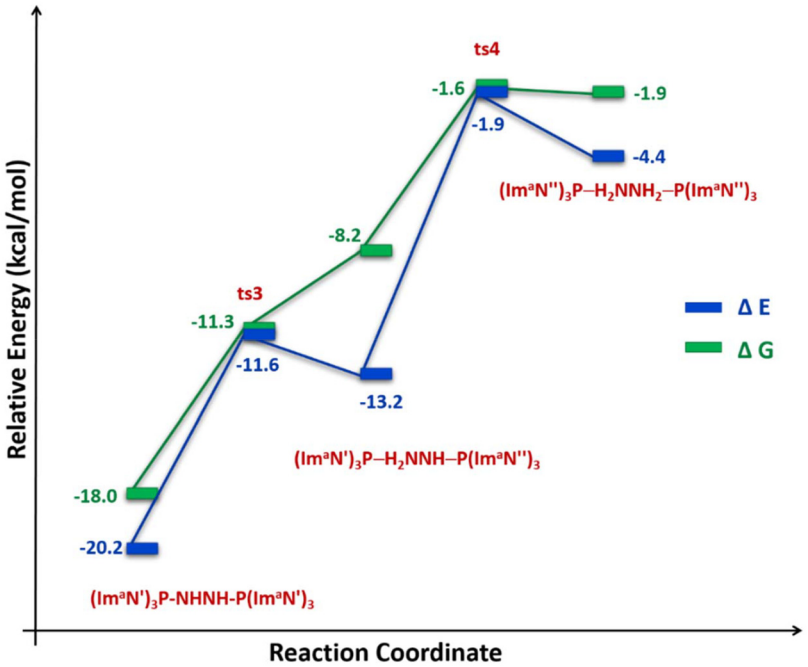

Fig. 11 Reaction energy profile diagram for hydrogen transfer occurs in **(Im^{a}N')$_3$P–HNNH–P(Im^{a}N')$_3$** to form the hydrazine complex **(Im^{a}N'')$_3$P–H$_2$NNH$_2$–P(Im^{a}N'')$_3$**.

(Im^{a}N'')$_3$P–H$_2$NNH$_2$ and has an energy change of 28.7 kcal mol^{-1} and a free energy change of 12.4 kcal mol^{-1}.

$$(\mathrm{Im^aN''})_3\mathrm{P–H_2NNH_2–P(Im^aN'')_3} \downarrow \quad (\mathrm{Im^aN''})_3\mathrm{P–H_2NNH_2} + \mathrm{P(Im^aN'')_3} \tag{2}$$

$$(\mathrm{Im^aN''})_3\mathrm{P–H_2NNH_2} \rightarrow (\mathrm{Im^aN''})_3\mathrm{P} + \mathrm{H_2NNH_2} \tag{3}$$

Comparing the energy profiles for diimine formation (Fig. 9) and hydrazine formation (Fig. 11) reveals that the diimine complex is both a kinetically and thermodynamically favoured product. However, the transformation from the diimine complex to the hydrazine complex, while endothermic, remains feasible due to its relatively low barrier of 18.3 kcal mol^{-1}. Furthermore, by strategically manipulating reaction conditions such as temperature, pressure, and reactant/product concentrations in accordance with Le Châtelier's principle, the equilibrium can be shifted to favour the formation of hydrazine, despite its thermodynamically less favoured nature.

Conclusions

This study presents a novel approach for N_2 activation using superbase phosphines, specifically $(ImN)_3P$. By leveraging the exceptional electron-donating ability of these newly designed ligands, we demonstrate a metal-free pathway for efficient N_2 activation, overcoming the challenges posed by the strong N–N triple bond.

DFT calculations at the M06L/6-311++G(d,p) level reveal that bis-phosphine complexes, forming hypervalent sandwich structures with N_2, exhibit the most promising N_2 activation. This activation is driven by the formation of strong P–N bonds with double bond character and a concomitant weakening of the N–N bond, as evidenced by structural and bonding analyses. The superbasic nature of the ImN-type substituents on the phosphine ligands plays a crucial role in enhancing their affinity for N_2 and stabilizing the resulting complexes.

We propose a two-step hydrogen transfer pathway for the $(ImN)_3P–N_2–P(ImN)_3$ sandwich complex, leading to the exothermic formation of a diimine intermediate with a significantly weakened N–N bond. Further hydrogen transfer results in the formation of a hydrazine complex, a process that, while endothermic, exhibits surmountable activation barriers.

This research underscores the potential of ImN-type superbase phosphine ligands in facilitating nitrogen activation and transformation. The ability to controllably convert dinitrogen into more reactive intermediates like diimine and hydrazine opens new avenues for the design of metal-free catalytic systems for nitrogen fixation and other applications in chemical synthesis. Experimental validation of these computational findings is the next crucial step in realizing the potential of this novel approach.

Author contributions

The manuscript was written through the contributions of all authors. All authors have read and approved the final version of the manuscript.

Data availability

The data supporting this study are available from the corresponding author upon reasonable request.

Conflicts of interest

There are no conflicts to declare.

Acknowledgements

VUK gratefully acknowledges the research fellowship (No. KSCSTE/972/2018-FSHP-MAIN) provided by the Kerala State Council for Science, Technology and Environment (KSCSTE), Kerala, India. CHS and VUK would also like to express their appreciation for the support received from the IT service unit of both CSIR-NIIST and CSIR-4PI institutes. Additionally, CHS extends his thanks to CSIR-NIIST for the opportunity to work on deputation assignment at SRIBS.

References

1 M. D. Fryzuk, J. B. Love, S. J. Rettig and V. G. Young, *Science*, 1997, **275**, 1445–1447.
2 S. D. Minteer, P. Christopher and S. Linic, *ACS Energy Lett.*, 2018, **4**, 163–166.
3 S. F. McWilliams, D. L. Broere, C. J. Halliday, S. M. Bhutto, B. Q. Mercado and P. L. Holland, *Nature*, 2020, **584**, 221–226.
4 V. Krewald, *Dalton Trans.*, 2018, **47**, 10320–10329.
5 S. L. Foster, S. I. P. Bakovic, R. D. Duda, S. Maheshwari, R. D. Milton, S. D. Minteer, M. J. Janik, J. N. Renner and L. F. Greenlee, *Nat. Catal.*, 2018, **1**, 490–500.
6 G. Qing, R. Ghazfar, S. T. Jackowski, F. Habibzadeh, M. M. Ashtiani, C.-P. Chen, M. R. Smith III and T. W. Hamann, *Chem. Rev.*, 2020, **120**, 5437–5516.
7 L. Wang, M. Xia, H. Wang, K. Huang, C. Qian, C. T. Maravelias and G. A. Ozin, *Joule*, 2018, **2**, 1055–1074.
8 C. J. M. van der Ham, M. T. M. Koper and D. G. H. Hetterscheid, *Chem. Soc. Rev.*, 2014, **43**, 5183–5191.
9 F. Neese, *Angew. Chem., Int. Ed.*, 2006, **45**, 196–199.
10 B. E. Smith, R. L. Richards and W. E. Newton, *Catalysts for nitrogen fixation: nitrogenases, relevant chemical models and commercial processes*, Springer Science & Business Media, 2004.
11 G. Schwarz, R. R. Mendel and M. W. Ribbe, *Nature*, 2009, **460**, 839–847.
12 K. M. Lancaster, M. Roemelt, P. Ettenhuber, Y. Hu, M. W. Ribbe, F. Neese, U. Bergmann and S. DeBeer, *Science*, 2011, **334**, 974–977.
13 B. M. Barney, H.-I. Lee, P. C. Dos Santos, B. M. Hoffman, D. R. Dean and L. C. Seefeldt, *Dalton Trans.*, 2006, 2277–2284.
14 B. M. Barney, T.-C. Yang, R. Y. Igarashi, P. C. Dos Santos, M. Laryukhin, H.-I. Lee, B. M. Hoffman, D. R. Dean and L. C. Seefeldt, *J. Am. Chem. Soc.*, 2005, **127**, 14960–14961.
15 L. C. Seefeldt, B. M. Hoffman and D. R. Dean, *Annu. Rev. Biochem.*, 2009, **78**, 701–722.
16 R. Y. Igarashi, M. Laryukhin, P. C. Dos Santos, H.-I. Lee, D. R. Dean, L. C. Seefeldt and B. M. Hoffman, *J. Am. Chem. Soc.*, 2005, **127**, 6231–6241.
17 F. Studt and F. Tuczek, *J. Comput. Chem.*, 2006, **27**, 1278–1291.
18 H. Broda, S. Hinrichsen and F. Tuczek, *Coord. Chem. Rev.*, 2013, **257**, 587–598.
19 B. M. Hoffman, D. R. Dean and L. C. Seefeldt, *Acc. Chem. Res.*, 2009, **42**, 609–619.
20 c. T. Bazhenova and A. Shilov, *Coord. Chem. Rev.*, 1995, **144**, 69–145.
21 C. Ling, X. Niu, Q. Li, A. Du and J. Wang, *J. Am. Chem. Soc.*, 2018, **140**, 14161–14168.
22 A. Shilov, *Russ. Chem. Bull.*, 2003, **52**, 2555–2562.
23 K. Arashiba, Y. Miyake and Y. Nishibayashi, *Nat. Chem.*, 2011, **3**, 120–125.
24 R. R. Schrock, *Nat. Chem.*, 2011, **3**, 95–96.
25 M. Yuki, H. Tanaka, K. Sasaki, Y. Miyake, K. Yoshizawa and Y. Nishibayashi, *Nat. Commun.*, 2012, **3**, 1254.
26 T. Mondal, W. Leitner and M. Hölscher, *Dalton Trans.*, 2024, **53**(18), 7890–7898.
27 M. Lan, N. Zheng, X. Dong, C. Hua, H. Ma and X. Zhang, *Dalton Trans.*, 2020, **49**, 9123–9129.
28 Y. Zhou, X. Yu, X. Wang, C. Chen, S. Wang and J. Zhang, *Electrochim. Acta*, 2019, **317**, 34–41.
29 P. Avenier, X. Solans-Monfort, L. Veyre, F. Renili, J.-M. Basset, O. Eisenstein, M. Taoufik and E. A. Quadrelli, *Top. Catal.*, 2009, **52**, 1482–1491.
30 N. Cao, Z. Chen, K. Zang, J. Xu, J. Zhong, J. Luo, X. Xu and G. Zheng, *Nat. Commun.*, 2019, **10**, 2877.
31 G. F. Chen, S. Ren, L. Zhang, H. Cheng, Y. Luo, K. Zhu, L. X. Ding and H. Wang, *Small Methods*, 2019, **3**, 1800337.
32 Y. Liu, Y. Su, X. Quan, X. Fan, S. Chen, H. Yu, H. Zhao, Y. Zhang and J. Zhao, *ACS Catal.*, 2018, **8**, 1186–1191.
33 F. Lü, S. Zhao, R. Guo, J. He, X. Peng, H. Bao, J. Fu, L. Han, G. Qi and J. Luo, *Nano Energy*, 2019, **61**, 420–427.
34 H. Iriawan, S. Z. Andersen, X. Zhang, B. M. Comer, J. Barrio, P. Chen, A. J. Medford, I. E. L. Stephens, I. Chorkendorff and Y. Shao-Horn, *Nat. Rev. Dis. Primers*, 2021, **1**, 56.
35 K. Edel, M. Krieg, D. Grote and H. F. Bettinger, *J. Am. Chem. Soc.*, 2017, **139**, 15151–15159.
36 M.-A. Légaré, G. Bélanger-Chabot, R. D. Dewhurst, E. Welz, I. Krummenacher, B. Engels and H. Braunschweig, *Science*, 2018, **359**, 896–900.
37 S. N. Shirodkar, C. A. Sayou Ngomsi and P. Dev, *ACS Appl. Electron. Mater.*, 2023, **5**, 1707–1714.
38 T.-T. Liu, D.-D. Zhai, B.-T. Guan and Z.-J. Shi, *Chem. Soc. Rev.*, 2022, **51**, 3846–3861.
39 B. Rösch, T. Gentner, J. Langer, C. Färber, J. Eyselein, L. Zhao, C. Ding, G. Frenking and S. Harder, *Science*, 2021, **371**, 1125–1128.

40 V. U. Krishnapriya and C. H. Suresh, *Organometallics*, 2023, **42**, 571–580.
41 F. B. Sayyed and C. H. Suresh, *J. Phys. Chem. A*, 2011, **115**, 9300–9307.
42 J. J. Chi, T. C. Johnstone, D. Voicu, P. Mehlmann, F. Dielmann, E. Kumacheva and D. W. Stephan, *Chem. Sci.*, 2017, **8**, 3270–3275.
43 F. Buss, P. Mehlmann, C. Mück-Lichtenfeld, K. Bergander and F. Dielmann, *J. Am. Chem. Soc.*, 2016, **138**, 1840–1843.
44 T.-F. Leung, D. Jiang, M.-C. Wu, D. Xiao, W.-M. Ching, G. P. Yap, T. Yang, L. Zhao, T.-G. Ong and G. Frenking, *Nat. Chem.*, 2021, **13**, 89–93.
45 C. H. Suresh, G. S. Remya and P. K. Anjalikrishna, *Wiley Interdiscip. Rev.: Comput. Mol. Sci.*, 2022, **12**, e1601.
46 S. R. Gadre and R. N. Shirsat, *Electrostatics of atoms and molecules*, Universities Press, 2000.
47 P. Politzer and D. G. Truhlar, *Chemical applications of atomic and molecular electrostatic potentials: reactivity, structure, scattering, and energetics of organic, inorganic, and biological systems*, Springer Science & Business Media, 2013.
48 C. H. Suresh and S. Anila, *Acc. Chem. Res.*, 2023, **56**, 1884–1895.
49 J. Tomasi, in *Quantum Theory of Chemical Reactions: 1: Collision Theory, Reactions Path, Static Indices*, Springer, 1979, pp. 191–228.
50 B. Galabov and P. Bobadova-Parvanova, *J. Phys. Chem. A*, 1999, **103**, 6793–6799.
51 C. H. Suresh and N. Koga, *Inorg. Chem.*, 2002, **41**, 1573–1578.
52 M. J. Frisch, G. W. Trucks, H. B. Schlegel, G. E. Scuseria, M. A. Robb, J. R. Cheeseman, G. Scalmani, V. Barone, G. A. Petersson, H. Nakatsuji, X. Li, M. Caricato, A. V. Marenich, J. Bloino, B. G. Janesko, R. Gomperts, B. Mennucci, H. P. Hratchian, J. V. Ortiz, A. F. Izmaylov, J. L. Sonnenberg, D. Williams-Young, F. Ding, F. Lipparini, F. Egidi, J. Goings, B. Peng, A. Petrone, T. Henderson, D. Ranasinghe, V. G. Zakrzewski, J. Gao, N. Rega, G. Zheng, W. Liang, M. Hada, M. Ehara, K. Toyota, R. Fukuda, J. Hasegawa, M. Ishida, T. Nakajima, Y. Honda, O. Kitao, H. Nakai, T. Vreven, K. Throssell, J. A. Montgomery, Jr., J. E. Peralta, F. Ogliaro, M. J. Bearpark, J. J. Heyd, E. N. Brothers, K. N. Kudin, V. N. Staroverov, T. A. Keith, R. Kobayashi, J. Normand, K. Raghavachari, A. P. Rendell, J. C. Burant, S. S. Iyengar, J. Tomasi, M. Cossi, J. M. Millam, M. Klene, C. Adamo, R. Cammi, J. W. Ochterski, R. L. Martin, K. Morokuma, O. Farkas, J. B. Foresman, and D. J. Fox, *Gaussian 16, Revision A.03*, Gaussian, Inc., Wallingford CT, 2016.
53 Y. Zhao and D. G. Truhlar, *Chem. Phys.*, 2006, **125**, 194101.
54 F. Weinhold and C. R. Landis, *Chem. Educ. Res. Pract.*, 2001, **2**, 91–104.
55 F. Weinhold, *Discovering chemistry with natural bond orbitals*, John Wiley & Sons, 2012.
56 P. Politzer and J. S. Murray, *Theor. Chem. Acc.*, 2002, **108**, 134–142.
57 S. R. Gadre, S. A. Kulkarni and I. H. Shrivastava, *J. Chem. Phys.*, 1992, **96**, 5253–5260.
58 N. Mohan, C. H. Suresh, A. Kumar and S. R. Gadre, *Phys. Chem. Chem. Phys.*, 2013, **15**, 18401–18409.
59 N. Mohan and C. H. Suresh, *J. Phys. Chem. A*, 2014, **118**, 1697–1705.
60 M. A. Wuensche, P. Mehlmann, T. Witteler, F. Buss, P. Rathmann and F. Dielmann, *Angew. Chem., Int. Ed.*, 2015, **54**, 11857–11860.